To date, high throughput dechlorination by membrane reactors has not been practical because of the conflicting requirements of high permeate flux and sufficient time for reaction within the membrane. High reactivity catalysts are needed to negotiate the conflicting demands of reactivity and throughput. We report on the design of metallic (Pd) and bimetallic (Pd-Au) catalysts supported on exfoliated graphite nanoplatelets (xGnPs) that enable TCE hydrodechlorination with rate constants up to 81 times higher than those obtained for the commercial Pd/Al_2O_3 catalyst. Nanocomposite membranes based on these novel catalysts can remove 96% of TCE at the high permeate flux of 47.4 $L/(m^2 \cdot h \cdot bar)$. An inexpensive alternative to graphene, xGnP-based catalyst supports can enable a broad range of other cost-efficient membrane reactions.

Pd and Pd-Au nanocatalysts supported on exfoliated graphite for high throughput dehalogenation by nanocomposite membranes

Revised version submitted for consideration as a publication in the *Environmental Science: Nano*

by

Christopher A. Crock and Volodymyr V. Tarabara*

Department of Civil and Environmental Engineering, Michigan State University, East Lansing, MI 48824, USA

Emails:

crockchr@msu.edu (C.A. Crock)

tarabara@msu.edu (V. V. Tarabara)

January 10, 2016

(original version submitted on November 8, 2015)

* Corresponding author

1

Abstract

Exfoliated graphite nanoplatelets (xGnPs) are proposed as a support material in the design of hierarchical Pd-based nanocatalysts for reductive dehalogenation. xGnP-supported metallic (Pd) and bimetallic (Pd-Au) catalysts were synthesized and evaluated in experiments on dehalogenation of trichloroethylene (TCE) in batch and membrane reactors.   The TCE removal of 96% was achieved with Pd-Au/xGnP-filled membranes operated at the specific permeate flux of 47.4 $L/(m^2 \cdot h \cdot bar)$.   Normalized reactive fluxes in flow-through dehalogenation by membranes with embedded Pd-Au/xGnP and Pd/xGnP catalysts were 14.71 ± 5.96 and 2.56 ± 1.79 $(m/s)(M_{H2})^{-1}(g_{Pd}/ g_{PSf})^{-1}$, respectively.   These values were ~80 and ~14 times higher than the normalized reactive flux obtained using membranes with embedded commercial Pd/Al_2O_3 catalyst.   To our knowledge, this is the first report on Pd and Pd-Au catalysts on a graphene-type support for hydrodechlorination and the first demonstration of high throughput TCE dechlorination in a membrane reactor. Determined for batch reactions, the second order reaction rate constants for Pd-Au/xGnP and Pd/xGnP catalysts were 26,309 ± 6,555 and 9,975 ± 9,506 $(M_{H2} \cdot s)^{-1}$ $(g_{Pd}/L)^{-1}$.   These values were ~81 and ~31 times higher than the rate constant obtained for the commercial Pd/Al_2O_3 catalyst.

Keywords: dehalogenation; exfoliated graphite nanoplatelets; bimetallic catalyst; palladium; supported catalyst; polymer nanocomposites

2

1. Introduction

Palladium-based catalysis has emerged as a promising approach to the reactive treatment of recalcitrant water pollutants such as halogenated organics [1, 2]. However, several technical challenges including low catalyst activity and fouling hinder field-scale applications of this technology.   Recent developments in nanocatalyst design for environmental applications have shown that catalyst support is important for highly selective and efficient reactions.   Graphene-supported Pd can be an excellent catalyst choice due to its good stabilities in both alkaline and acid conditions and graphene's unique electronic properties where electron shuttling between the support and the metal could improve reactivity [3-6]. Other properties of graphene that are purported to explain its very good properties as a catalyst support include accessibility of reactants to active centers due to the graphene's 2D morphology [7] as well as various specific interactions between reactants and graphene's surface [3, 8].   Graphene as a support has been shown to increase catalytic activity of Pd in the Suzuki reaction [9].   In the electrooxidation of formic acid and ethanol, graphene-supported Pd had much higher catalytic activity and better stability than commercial Pd/carbon catalysts [10].   In the dehydrogenation and hydrolysis of ammonium borane, graphene-supported Pd was also shown to be more active and stable than commercial counterparts [11]. Adsorption of the reactants to the carbon surface may also be contributing to increased reactivity [12].

Stacked sheets of reduced graphene, exfoliated graphite nanoplatelets (xGnP) have surface properties very similar to those of graphene, offer high surface area (up to 750 m^2/g), and are more affordable with the expected cost on the order of $5/pound [13,14]. Ranging from 2 to 12 nm in thickness and several microns in diameter, xGnPs can be viewed as pseudo two-dimensional nanoplatelets offering functionality of graphene at a lower cost.   In contrast to activated carbon, xGnPs are not microporous; catalytic nanoparticles can be anchored on the xGnP's basal plane

making them readily available to reactants.   xGnPs have been used as catalyst support in the past: Lu et al. reported on the synthesis and application of Pt and Pd nanoparticles on xGnPs for catalytic redox reactions involving H_2O_2 [15] while Maiyalagan et al. [16] used chemically modified xGnPs as support for Pd and Pd-Au catalysts in formic acid oxidation. We used xGnPs modified by nanoAu as components of membrane casting mixtures and demonstrated that resulting porous asymmetric nanocomposites were permselective and catalytically active ultrafiltration membranes [17].

Table 1:   Literature data on the reactivity of various Pd-based catalysts in batch dehalogenation of TCE with H_2 as the reducer.
[a] Using a Pd content of 41.1 wt%
[b] Designed with the optimal Pd content of 12.7 wt%
[c] CMC = sodium carboxymethylcellulose

	Promoter	Support	k_{obs}, $\frac{1}{min}\frac{1}{\frac{gPd}{L}}$	Reference
Pd	–	–	55	Nutt et al., 2006 [18]
Pd-Au	Au	–	433 [a] and 1956 [b]	
Pd/Al_2O_3	–	Al_2O_3	12.2	Nutt et al., 2005 [19]
CMC[c]-capped Pd	–	–	828	Liu et al., 2008 [20]
Bio Pd	–	*S. oneidensis*	$4.0\cdot10^{-4}\pm3.3\cdot10^{-6}$	De Corte et al., 2011 [21]
Bio Pd-Au	Au	*S. oneidensis*	$1.3\cdot10^{-3}\pm1.6\cdot10^{-4}$	

Optimizing the materials design of catalysts can prevent catalyst poisoning and improve reaction rates.   In recent studies, bi- and tri-metallic catalysts for reductive reactions were synthesized and their reactivities were measured [18, 19, 22-26].   Table 1 lists Pd-based metallic and bimetallic catalysts that were evaluated in the reductive dechlorination of TCE with dissolved hydrogen as the reducer.   All these studies employed 1st order reaction kinetics to describe TCE dehalogenation.   Bimetallic Pd-on-Au nanocatalysts showed improved catalytic efficiency due to the Au promoter and were optimized for TCE dechlorination [19].   It was later demonstrated that the

extent of coverage of Au nanoparticles by Pd regulated the efficiency of catalytic reduction of TCE and that Au eliminated sulfide poisoning of the catalyst [18]. Compared to Pd catalysts supported on Al_2O_3, the Pd-on-Au catalysts with optimized Pd coverage increased the first order rate constant from 47 $min^{-1} \cdot (g_{Pd}/L)^{-1}$ to 1956 $min^{-1} \cdot (g_{Pd}/L)^{-1}$ [18]. Bimetallic Pd-Fe systems can also be used to catalytically reduce chlorinated organics wherein hydrogen is generated in situ [25, 27-29].

Another study successfully applied Langmuir-Hinshelwood model to quantify TCE reaction kinetics [30]; although more appropriate than simpler models, Langmuir-Hinshelwood kinetics could not be applied in our case as the model relies on several assumptions (e.g. constant TCE concentration) that did not hold in the present study.
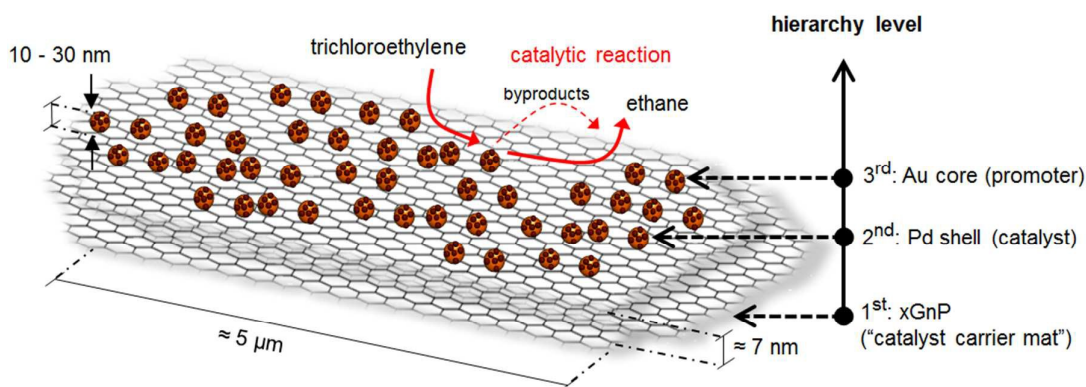

Figure 1:   Conceptual illustration of a hierarchical nanocatalyst based on bimetallic (Pd-Au) as catalytic nanoparticles and exfoliated graphite nanoplatelets (xGnP) as catalyst support. The Pd-Au nanoparticles have core-shell morphology with Au and Pd forming the core and the shell, respectively.

Using membrane reactors for catalysis can be advantageous in several aspects. First, in catalytic membranes the diffusional limitation is mitigated due to the small size of pores and the rate of mass transfer of pollutants to the catalyst surface can be regulated by the rate of permeation [31]. A rough estimate shows that the typical size of ultrafiltration membrane pores (2 to 100 nm) is much smaller than the diffusional

distance, δ_{diff}, for TCE ($D = 8.16 \cdot 10^{-10}$ m^2/s at 25 ^{0}C [32]) or a similar molecule over the typical detention time in a dense sublayer of an ultrafilter ($t_{det} \sim 0.2$ to 5 s):

$\delta_{diff} \cong \sqrt{Dt_{det}} = 5$ to 23 µm. In this regard, membrane reactors hold an advantage over packed bed reactors with pores that are several orders of magnitude larger than pores in an ultrafiltration membrane. Second, reactive membranes obviate the need to recover the catalyst. Third, membrane reactors may eliminate catalyst poisoning or fouling by rejecting foulants at the feed-membrane interface. Immobilizing catalysts on various supports prior to incorporating them into membranes enables better catalyst dispersion throughout the membrane [17, 33] and may minimize catalyst loss to the permeate flow.

This paper reports on the preparation of two novel Pd-based catalysts on an exfoliated graphite support for TCE hydrodechlorination (Figure 1). We have fabricated Pd/xGnP and Pd-Au/xGnP catalysts and compared them against the commercial Pd/Al$_2$O$_3$ catalyst in a batch reactor and as components of polymer nanocomposite membranes in a membrane reactor. To our knowledge, this is the first report on Pd and Pd-Au catalysts on a graphene-type support for hydrodechlorination and the first demonstration of TCE dechlorination in a flow-through membrane reactor.

6

2. EXPERIMENTAL

2.1 Reagents

Ethylene glycol (EG) (Fluka), sodium hydroxide pellets (Fluka), 20 wt% aqueous solution of poly(diallyldimethylammonium) chloride (PDADMAC) (Sigma Aldrich), TCE (Sigma Aldrich), and Pd on alumina (5wt% Pd) (Sigma Aldrich), palladium chloride ($PdCl_2$) (Sigma Aldrich) and gold (III) chloride trihydrate ($HAuCl \cdot (H_2O)_3$) (Sigma Aldrich) were used as precursors in Pd and Au nanoparticle synthesis. Hydrogen (99.9% purity) and nitrogen (99.99% purity) gases were used to saturate TCE feed solutions.

2.2. Synthesis of Pd/xGnP and Pd-Au/xGnP nanocatalysts and nanocomposite membranes

All chemicals were used as received. Exfoliated graphite nanoplatelets (grade M; XG Sciences) were used as a support for Pd and Pd-Au nanoparticles. The nanoplatelets were ~ 7 nm thick with the average diameter of 5 µm and surface area in the 120 to 150 m^2/g range. Pd and Pd-Au nanoparticles on the xGnP support were fabricated by thermal reduction using polyol synthesis with ethylene glycol (EG) as a reducing agent.

2.2.1 Au/xGnP fabrication process

To make Au/xGnP, 50 mg of xGnP was added to a mixture containing 50 mL of EG and 1 mL of a 20 wt% aqueous solution of polydiallyldimethylammonium chloride and dispersed in a sonication bath for 12 h. Next, 150 µL of 1 M NaOH and 50 µL of 500 mM $HAuCl_4$ were added to the xGnP suspension. NaOH was used to adjust the pH, which has been shown to control the size and morphology of the resulting Au nanoparticles [17]. The suspension was mixed and heated to maintain its temperature at 195 ˚C (near the boiling point of EG, 197 ˚C) for 30 min. Finally, Au/xGnP

7

nanoparticles were removed from EG by centrifugation, washed with acetone 3 times, and allowed to dry overnight in an oven at 100 ˚C.

2.2.2 Pd/xGnP and Pd-Au/xGnP fabrication process

To make Pd/xGnP and Pd-Au/xGnP, 50 mg of neat xGnP (or Au/xGnP) was dispersed in 18 mL of EG in a sonication bath (Aquasonic 50T, VWR Scientific) for 12 h.   Next, 2 mL of 22.5 mM Pd precursor solution was added to 18 mL of the xGnP suspension in EG and stirred for 2 min.   To reduce the precursor to Pd nanoparticles on the xGnP (or Au/xGnP) surface, the stirred suspension was microwaved for 50 s (900 W, 2450 MHz).   Finally, Pd/xGnP (or Pd-Au/xGnP) nanoparticles were removed from EG by centrifugation, washed with acetone 3 times, and allowed to dry overnight in an oven at 100 ˚C.

2.2.3 Characterization of Pd/xGnP and Pd-Au/xGnP catalysts by TEM, S-TEM, and S-TEM EDS

Transmission electron microscopy (TEM) imaging and scanning-TEM (S-TEM) energy dispersive X-ray spectroscopy (EDS) mapping were performed using a JOEL 2200FS microscope.   Nanoparticle specimens were prepared by dispersing nanoparticles in acetone (~0.01 wt%).   The nanoparticles were dispersed by bath sonication and a drop of nanoparticle suspension was placed on a 300-mesh nickel or copper grid.   The grid dried for 24 h at 90 ˚C prior to TEM imaging and S-TEM EDS mapping.   The Pd and Au contents were quantified using an atomic absorption (AA) analyzer (Perkin–Elmer 1100).

2.3 Preparation of nanocomposite membranes filled with Pd/xGnP and Pd-Au/xGnP catalysts

The procedure for casting polysulfone nanocomposite membranes filled with Pd/xGnP and Pd-Au/xGnP was similar to the one described previously [17].   Briefly, membranes were prepared using a combination of wet and dry phase inversion.

The relative concentrations of N-methyl-2-pyrrolidone (70 wt%), polysulfone (15 wt%), and PEG400 (15 wt%) of the casting mixture were the same for all membranes. The loading of Pd/xGnP or Pd-Au/xGnP in the membrane was 2 wt% of the PSf content while the loading of Pd/Al$_2$O$_3$ was 10 wt% of the PSf content.

The membrane preparation procedure included the following six steps:

1) Supported nanocatalysts were dispersed in NMP and sonicated for 2 h in a bath sonicator (model 50T, VWR Aquasonic).
2) PSf and PEG400 were added to the dispersion of xGnP-supported catalyst in NMP and the resulting mixture was stirred at 60 ˚C for 24 h.
3) The resulting mixture was cooled to room temperature and then cast onto a glass substrate using a film applicator (model 3570, Elcometer).
4) The cast film was exposed to air to allow NMP to evaporate for 30 s and then immersed into a water bath at room temperature.
5) After phase inversion was complete (as manifest by the separation of the cast film from the glass substrate) residual NMP was removed from the membrane by rinsing it with DI water for 5 min. The membrane was then soaked in DI water for 24 h to ensure complete removal of NMP.

After soaking, the water was exchanged and the membrane was stored wet at 4 ˚C until further use.

2.4. TCE dechlorination experiments

Before dechlorination experiments, controls were run to ensure that hydrogen would not leak from the batch reactor vessel and flow-through reactor feed vessel. This was done by monitoring the hydrogen concentration with for 6 h in both reactor vessels and no measureable loss of dissolved hydrogen was detected.

2.4.1 TCE dechlorination experiments: batch reactor tests

Nanocatalyst reactivity for TCE dechlorination was first characterized in zero-headspace batch reactor tests.   Serum vials were completely filled with 108 mL of high purity water (> 10 MΩ·cm^{-1}), and the water was purged of dissolved oxygen by bubbling nitrogen gas (99.99% purity) through the water with a ceramic frit for 15 min. After removing dissolved oxygen, 1.25 mg of either Pd/xGnP or Pd-Au/xGnP nanoparticles, or 64 mg of Pd/Al$_2$O$_3$ were added to the vial.   The different catalyst concentration of Pd/Al$_2$O$_3$ was chosen in order to enable measurements of TCE concentration by gas chromatography.   The solution in the vial was saturated (0.8 mM) with H$_2$ gas (99.9% purity) for 15 min at room temperature under atmospheric pressure and sealed with a Teflon septum and crimp cap.   Injecting 1 mL of 1000 mg/L stirred aqueous solution of TCE started the reaction. The batch reactor was magnetically stirred. Each sample withdrawn from the reactor was passed through a 0.22 μm syringe filter to remove the catalyst and terminate the reaction.   The extent of TCE reduction was measured by gas chromatography with an electron capture detector (see Supplementary Material (SM), section S1, for details).   Control experiments were conducted without H$_2$ and it was shown that there was no observable adsorption of TCE on xGnP (see SM, Figure S1).   The reactive loss of TCE should be only to the reaction within the intrapore space of the membrane. That is because the loose ultrafiltration membranes (MWCO of ~ 90 kDa) used in this work should not reject TCE and there should be no TCE concentration boundary layer at the feed face of the reactive membrane surface. The concentration of dissolved H$_2$ was determined using an H$_2$ electrode microsensor and a picoampere-range amplifier (Unisense H2-NP).

2.4.2 TCE dechlorination experiments: flow-through tests with a membrane reactor

Flow-through dechlorination experiments were conducted using a dead-end filtration system (Figure 2) that included a stirred filtration cell (model 8050, EMD Millipore),

10

stirring plate, mass balance, stainless steel pressure vessel, and hermetic plastic bladder (High Sierra). An H_2 sensor and signal amplifier were used for H_2 monitoring. To avoid exposure of the H_2-saturated feed solution to the atmosphere and to the inner surface of the pressure vessel, the solution was poured into a hermetic bladder, which was then placed inside the pressure vessel and pressurized while still hermetically sealed. Testing of the bladder for H_2 leakage showed no loss of H_2 and over a period of 6 h.
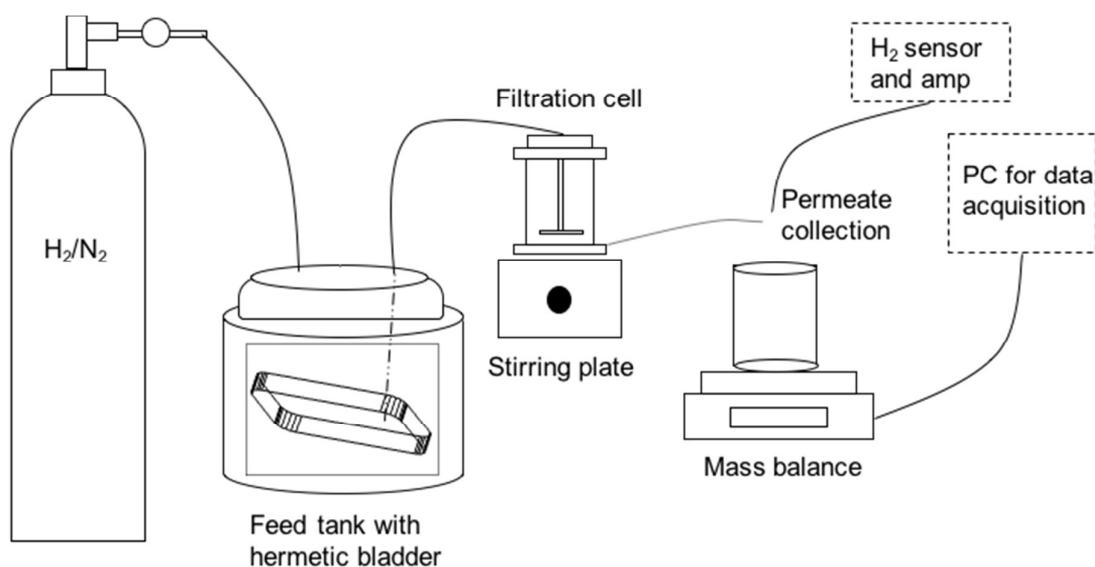

Figure 2: Schematic of the dead-end filtration system used in TCE dechlorination experiments.

Prior to measuring membrane reactivity, membrane adsorption capacity was exhausted by filtering a 9.25 mg/L TCE solution in the absence of reaction. Then, the reactivity was determined in ultrafiltration of a 9.25 mg(TCE)/L feed solution saturated with hydrogen. A survey of literature showed that TCE was typically found in groundwater at concentrations of mg/L [34]; the specific value (9.25 mg/L) was chosen on the basis of the "trial-and-error" preliminary screening study. The determination of catalytic activity included the following steps:

1) 1 L of DI water was added to a plastic bladder (High Sierra) and purged with $N_2(g)$ for 15 min.

11

2) 10 mL of 1000 mg/L TCE solution was added to N_2-purged water in the bladder, all headspace was removed, and the bladder was sealed.

3) The bladder was placed in a 5 L stainless steel pressure vessel (Alloy Products); the vessel was pressurized and the TCE solution was filtered through the membrane in four steps with a different transmembrane pressure at each step: 40, 30, 20, and 10 psi. The details of how the reaction rate constant for the membrane reactor can be calculated based on the results of tests with different transmembrane pressures can be found elsewhere [17].

4) Step 3 was repeated, except that the N_2-purged water was saturated with hydrogen prior to the addition of the TCE solution, and the aqueous hydrogen concentration of the permeate was monitored using an H_2 electrode microsensor and a picoampere-range amplifier. The permeate was collected in glass vials that were then sealed with Teflon lined caps.

5) TCE concentration in permeate samples was determined using gas chromatography.

3. Results and Discussion

3.1. Pd/xGnP and Pd-Au/xGnP nanocatalysts

We evaluated several approaches to the preparation of xGnP-supported Pd and Pd-Au nanocatalysts.   The most active bimetallic catalyst resulted from a hybrid procedure that combined features of two previously reported techniques [17, 35]; the procedure included two steps: 1) decoration of the xGnP support by Au nanoparticles using thermal reduction in an oil bath, followed by 2) deposition of Pd via microwave-assisted thermal reduction.   TEM images of catalyst-modified xGnPs show that most (~87%) Pd nanoparticles were in 5 nm to 10 nm size range and that most (~85%) Pd-Au nanoparticles were in 10 nm to 30 nm size range (Figure 1). Both metallic and bimetallic nanoparticles were distributed over xGnPs with minimal surface aggregation (see SM, section S7, for size distribution details).   EDS showed that both Pd and Au were present on the xGnP support with relative atomic concentrations of 60% and 40%, respectively, and AA spectroscopy corroborated the EDS data (see SM, Figure S2, Table S1).   S-TEM EDS mapping was employed to further probe the morphology of the Pd-Au nanoparticles anchored on xGnP supports and elucidate the relative distribution of the two metals in the catalyst particles.   The mapping pointed to the "core-shell" morphology with Au forming the core and Pd forming the shell, where the relative strength of the Pd signal is weaker in the center and stronger on the periphery while the Au signal is weaker on the periphery and stronger in the center of the particle (Figure 3).   This morphology is expected based on the sequence of steps in the catalyst preparation procedure (i.e. formation of Au nanoparticles followed by Pd deposition).   Because of the semi-quantitative nature of S-TEM EDS technique, it was not possible to determine what shell and core thicknesses were and whether the shell was a continuous layer of Pd or "islands" of Pd decorating the Au core.
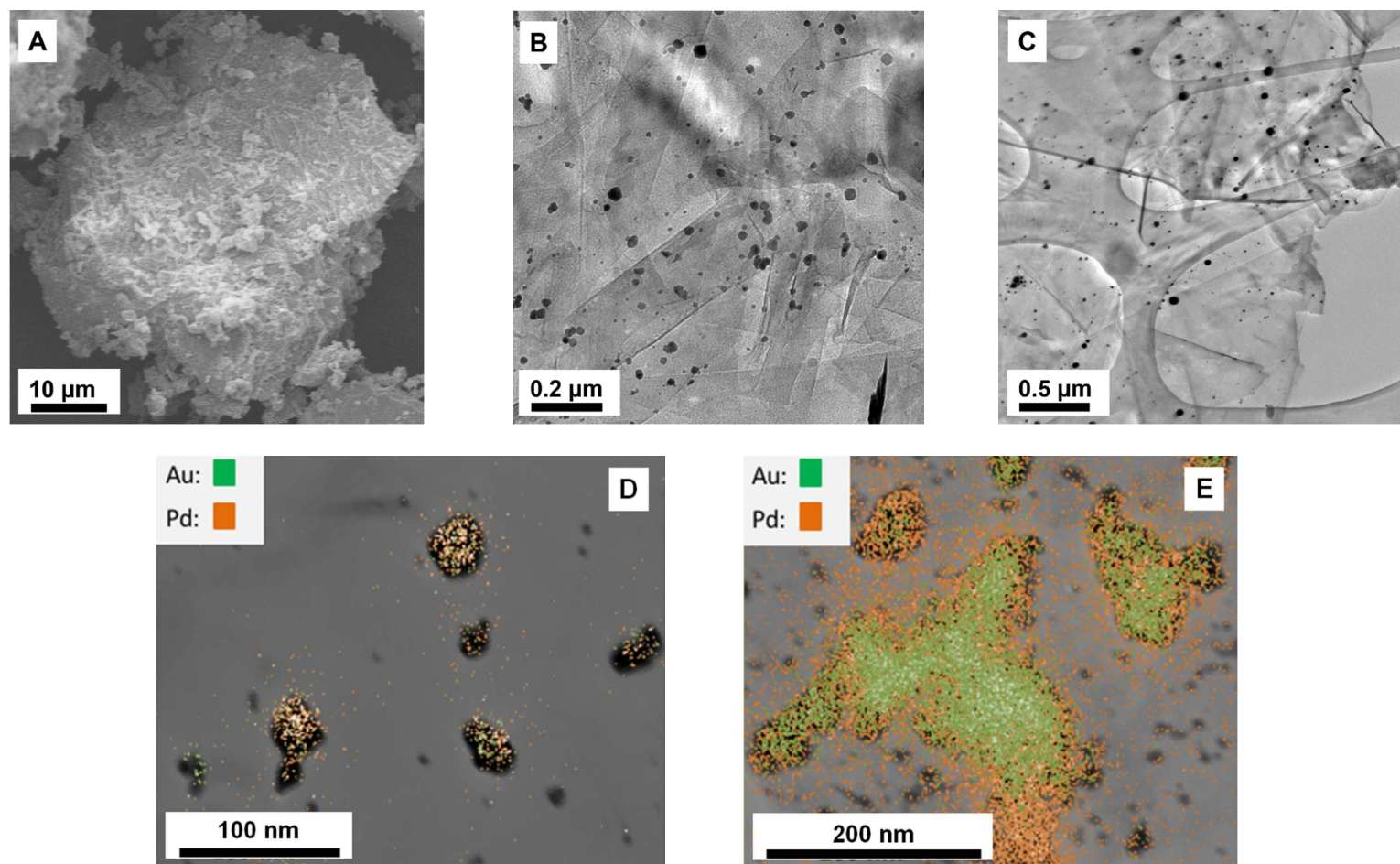
Figure 3: SEM (a), TEM (b, c) and S-TEM (d, e) images of the catalysts: (A) commercially available Pd/Al$_2$O$_3$ (Sigma-Aldrich); (B) newly synthesized Pd/xGnP; (C, D, E) newly synthesized Pd-Au/xGnP. The mapped distributions of Pd and Au (D, E) are representative of all Pd-Au/xGnP particles probed by S-TEM EDS.

14

In our previous work on Au/xGnP catalysts embedded within membranes of the same formulation, we showed that the catalyst is homogeneously distribution within polymeric UF membrane matrix. Because the catalysts are morphologically indistinguishable, Pd/xGnP and Pd-Au/xGnP should also be distributed homogeneously.

3.2. Kinetics of catalytic dehalogenation of TCE in batch reactors

The catalytic reactivity of Pd/xGnP and Pd-Au/xGnP was first characterized in experiments on the reduction of TCE in a batch reactor.   The concentration of H_2 was found to decrease according to 1st order kinetics (see SM, Figure S5):

$$[H_2] = [H_2]_0 \exp(-\varkappa^{batch} t) \tag{1}$$

where $\varkappa^{batch}$ (s^{-1}) is the reaction rate constant. For example, the average value of $\varkappa^{batch}$ in tests with Pd-Au/xGnP catalyst was $3.43 \cdot 10^{-3}$ s^{-1}.   Because of the decomposition of H_2, the TCE reaction data fit a 2nd order model (see SM, Figure S3) better than 1st order and 2nd order reaction rate constants were extracted for Pd/Au, Pd/xGnP, and Pd/Al$_2$O$_3$ catalysts.   We note that in all prior studies TCE dechlorination was modeled as a 1st order reaction [18-21] (Table 1) making direct comparison with our data on 2nd order kinetics not possible.   The batch process was modeled as a 2nd order reaction in an ideal reactor:

$$\frac{d[TCE]}{dt} = -k_{obs}^{batch}[TCE][H_2] \tag{2a}$$

Integration of (1) and (2a) gives:

$$ln\frac{[TCE]}{[TCE_0]} = -k_{obs}^{batch}\frac{[H_2]_0}{\varkappa^{batch}}\{1 - exp(-\varkappa^{batch} t)\} \tag{3a}$$

The normalized observed TCE reaction rate constant in batch dehalogenation, $\hat{k}_{obs}^{batch}$ (($M_{H2} \cdot s$)$^{-1}$ (g_{Pd}/L)$^{-1}$)), was computed by dividing k_{obs}^{batch} (($M_{H2} \cdot s$)$^{-1}$) by Pd content in the reactor. To our knowledge, the present study is the first description of catalytic hydrodechlorination of TCE as a 2nd order reaction.
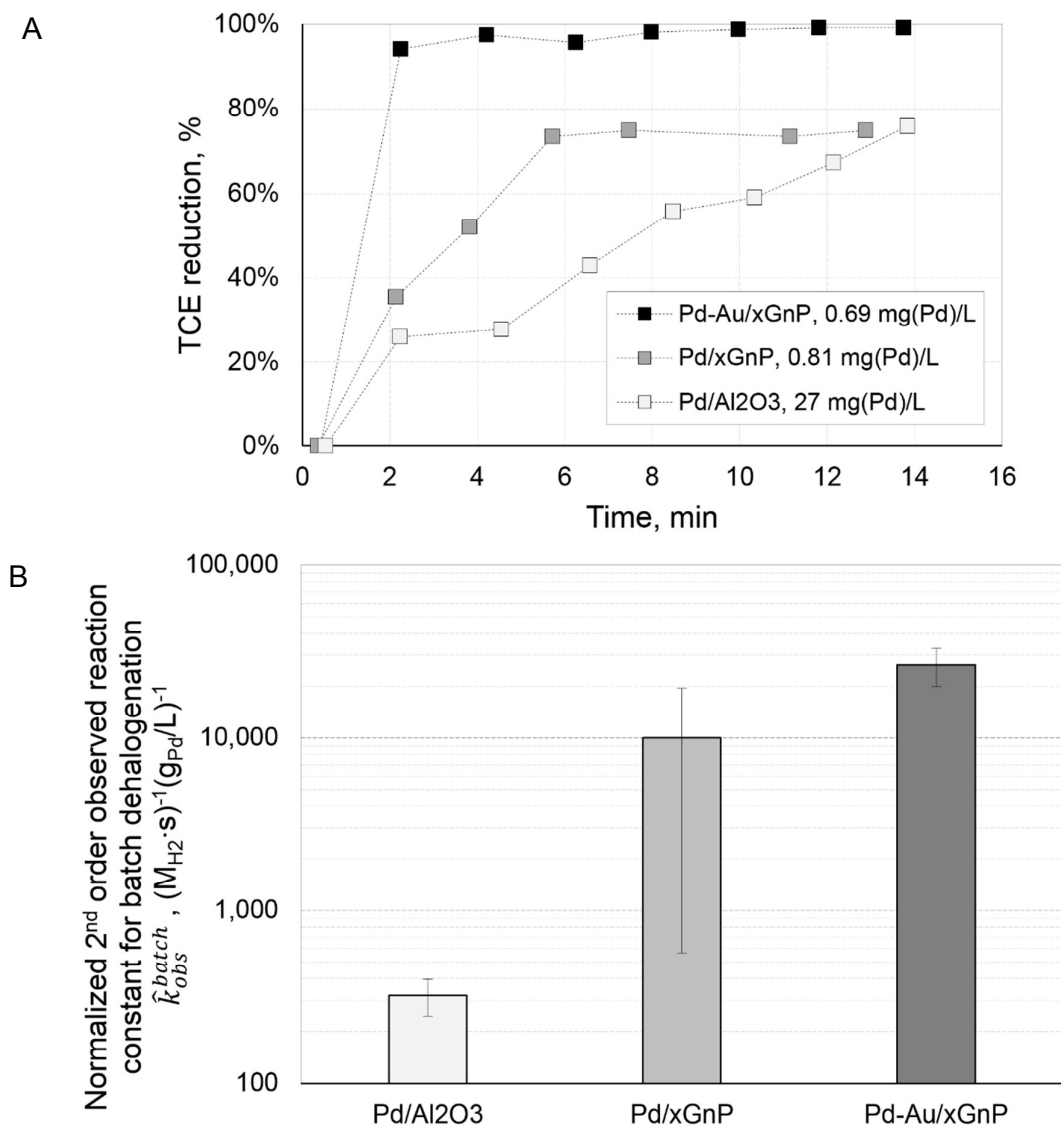
15

Figure 4: TCE dehalogenation performance of xGnP-supported Pd and Pd-Au catalysts and the commercial Pd/Al$_2$O$_3$ catalyst in batch reactions: A) Example data on TCE reduction. Pd content in the batch reactors is shown in the legend. B) 2nd order reaction rate constants normalized by the Pd content in the batch reactor for the three catalysts.   The errors correspond to the 95% confidence interval.

We emphasize that the choice of the 2nd order kinetics to describe the reaction is based on the experimental fact that the concentration of the reducing agent is decreasing ($\varkappa^{batch} \neq 0$, Figure S5) and, generally, cannot be assumed constant.

Small differences in the Pd content in tests with Pd/xGnP and Pd-Au/xGnP (0.69 mg(Pd)/L vs 0.81 mg(Pd)/L) were due to differences in the Pd content of these two catalyst types. The same mass (1.25 mg, see section 2.4.1) of each supported catalyst was added to batch reactors but the contents of Pd in Pd/xGnP and in Pd/xGnP were slightly different.

We extracted catalytic reaction rate constants for Pd-Au/xGnP, Pd/xGnP, and Pd/Al_2O_3 from the nearly 15 min of reaction time (Figure 4A).   More than 90 % of TCE was reduced within 15 min of the reaction catalyzed by Pd-Au/xGnP. In contrast, in tests with Pd/xGnP the TCE reduction plateaued near 80% and in tests with Pd/Al_2O_3 TCE reduction was even less complete. Figure 4B summarizes data on the reactivity of the two novel xGnP-supported catalysts and of the commercial Al_2O_3-supported Pd in a batch reactor.   The 2nd order reaction rate constants for Pd/xGnP (9,975 ± 9,506 $(M_{H2} \cdot s)^{-1}(g_{Pd}/L)^{-1}$) and Pd-Au/xGnP (26,309 ± 6,555 $(M_{H2} \cdot s)^{-1}(g_{Pd}/L)^{-1}$), were ~ 31 times and ~ 81 times higher than that for the commercial Pd/Al_2O_3 catalyst (321 ± 77 $(M_{H2} \cdot s)^{-1}(g_{Pd}/L)^{-1}$).

While by-products of the reaction were not monitored in this study, byproduct analysis is important for ensuring the reaction is complete and no toxic by-products (e.g. dichloroethenes and vinyl chloride) remain. Such information might also provide additional mechanistic insights into reaction pathways although the effect of byproducts is likely mitigated by the fact that the reduction of TCE to DCE is the limiting reaction in the overall catalytic hydrodechlorination process [30].

3.2.1. Dehalogenation kinetics in the batch reaction with a near-constant concentration of the reducing agent.

Because of practical limits on the sampling time (i.e. finite time needed for sample withdrawal and filtration, H_2 measurement, and sample transfer to gas chromatography vials for TCE measurement), we were unable to record TCE concentration during the earliest stages (< 2 min) of the reaction. Yet for highly active catalysts such as Pd-Au/xGnP, TCE concentration decreased dramatically (~ 90%) over the first 2 min.　To quantify reaction kinetics when TCE reduction was < 90%, we performed additional batch tests with a 5 times lower catalyst content. The experiments showed (see SM, section S4) that for low levels of TCE reduction, a 1st order model provided a good fit.　This was because sufficiently early into the experiment ($\varkappa^{batch} t \ll 1$), the 2nd order reaction given by eq. 1a reduced to a 1st order reaction:

$$\frac{d[TCE]}{dt} = -k_{obs}^{batch}[TCE][H_2]_0 \exp(-\varkappa^{batch}t) \xrightarrow{\varkappa^{batch}t \to 0} k_{1obs}^{batch}[TCE] \tag{2b}$$

where k_{1obs}^{batch} is the observed 1st order rate constant in the batch reactor.　We note that for reactions where the reducing agent (H_2 in our case) is reacting away sufficiently slowly, the 1st order kinetics can apply even late into the reaction:

$$\lim_{\varkappa^{batch} \to 0} \frac{1 - exp(-\varkappa^{batch}t)}{\varkappa^{batch}} = t \tag{4}$$

and

$$ln\frac{[TCE]}{[TCE_0]} = -k_{obs}^{batch}\frac{[H_2]_0}{\varkappa^{batch}}\{1 - exp(-\varkappa^{batch}t)\} \xrightarrow{\varkappa^{batch} \to 0} -k_{1obs}^{batch}t \tag{3b}$$

We extracted both 1st and 2nd order rate constants for batch reactors, and these constants, when normalized by Pd content, were not statistically different from respective rate constants measured in batch reactions with higher content of Pd-Au/xGnP.　Specifically, for high and low Pd-Au/xGnP contents the 1st order rate constants, $\hat{k}_{obs}^{batch}$, were 311 ± 120 and 559 ± 121 L/(min·g$_{Pd}$)$^{-1}$, respectively, and the

2nd order rate constants, $\hat{k}_{obs}^{batch}$, were 26,309 ± 6,555 and 18,255 ± 9,008 $(M_{H2} \cdot s)^{-1}(g_{Pd}/L)^{-1}$, respectively.

Although the 1st order batch reaction model gives an inferior fit to experimental results (i.e. inferior to the fit provided by the 2nd order batch reaction model described by eq. (3)), we applied it to our batch TCE dehalogenation data in order to compare the Pd-Au/xGnP and Pd/xGnP catalytic reactivity with reaction rate constants reported in the literature (Table 1). The 1st order reaction rate constants for Pd-Au/xGnP and Pd/xGnP catalysts (311 and 140 $L/(min \cdot g_{Pd})^{-1}$, respectively) are within an order of magnitude of the highest reaction rate constants reported earlier[18] even with no optimization of the Pd:Au surface coverage. We also note that because of their hydrophobicity, xGnPs could not be fully dispersed in the aqueous solution of TCE; it is likely that the efficiency of the reaction can be significantly enhanced by a better dispersion of the xGnP-supported catalysts.

3.3. Kinetics of catalytic dehalogenation of TCE in flow-through membrane reactors

The membrane-based dehalogenation of TCE by composite membranes was modeled as a 2nd order reaction in an ideal plug-flow reactor at steady-state:

$$0 = -v\frac{d[TCE]}{dx} - k_{obs}^{mem}[TCE][H_2] \qquad (5a)$$

where v (m/s) is the superficial velocity (i.e. permeate flux). As in batch tests, H_2 was found to react away according to a 1st order reaction in a plug flow reactor (see SM, Figure S4) so that H_2 decomposition was modeled as:

$$[H_2] = [H_2]_0 \exp(-\varkappa^{mem}\ell_{eff}/v) \qquad (6)$$

where $\varkappa^{mem}\ell_{eff}$ (m/s) is the reactive flux of H_2 in the membrane. Integration of (5a) and (6) gives:

$$ln\frac{[TCE]}{[TCE]_0} = -k_{obs}^{mem}\ell_{eff}\frac{[H_2]_0}{\varkappa^{mem}\ell_{eff}}\{1 - exp(-\varkappa^{mem}\ell_{eff}/v)\} \qquad (7a)$$
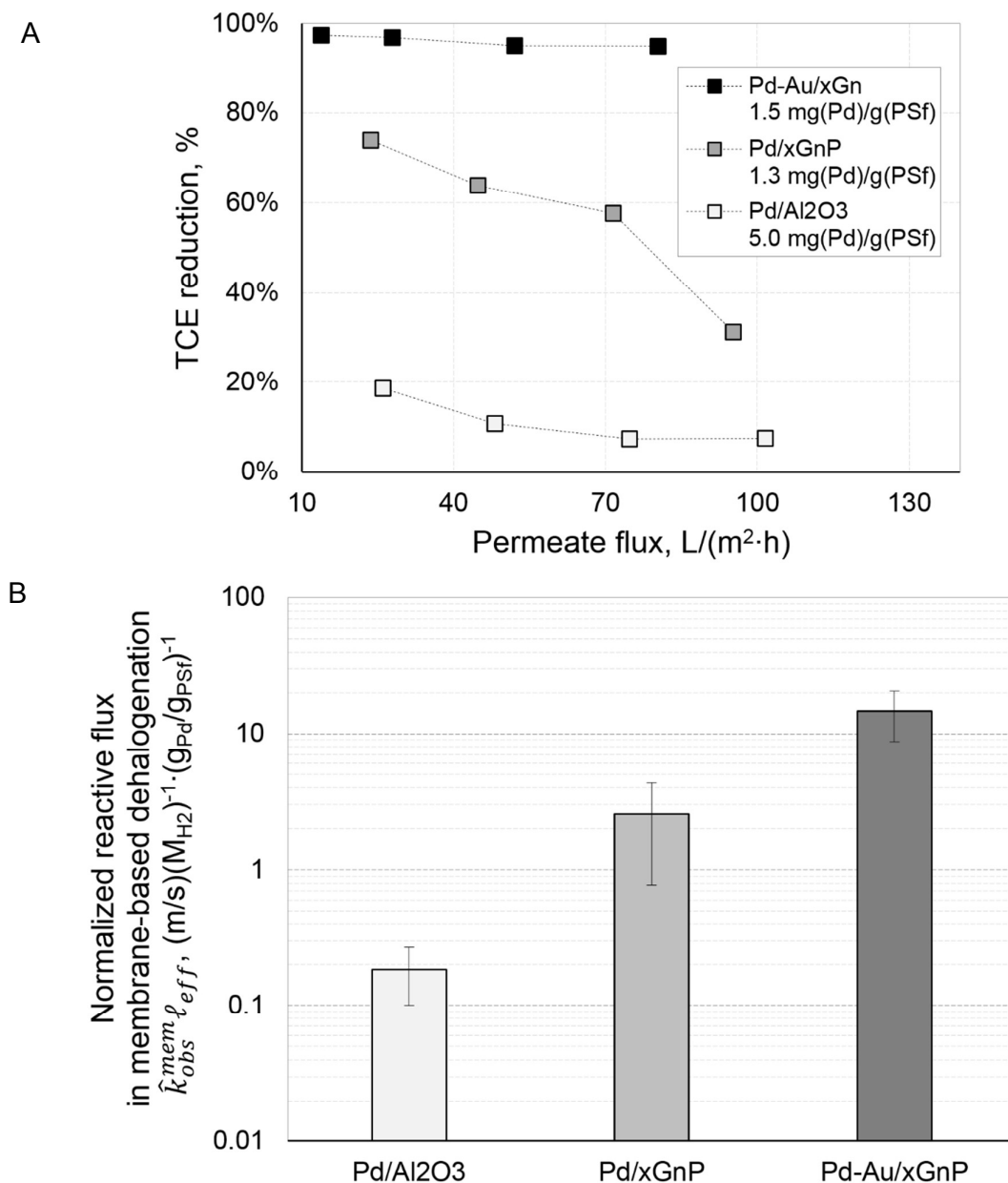
19

Figure 5: TCE dehalogenation performance of xGnP-supported Pd and Pd-Au catalysts and the commercial Pd/Al₂O₃ catalyst in flow-through membrane reactors:

A) Example data on TCE reduction in membrane filtration tests. Pd loading in nanocomposite membranes is shown in the legend. The four points in each data set correspond to transmembrane pressure values of 10, 20, 30, and 40 psi.

B) Normalized reactive fluxes in membrane dehalogenation by nanocomposite membranes with embedded catalysts. The errors correspond to the 95% confidence interval.

where ℓ_{eff} is the effective length of the reactor and $k_{obs}^{mem}\ell_{eff}$ $((m/s)(M_{H2})^{-1})$ is the reactive flux of TCE in the membrane.

The reactive fluxes $k_{obs}^{mem}\ell_{eff}$ and $\varkappa^{mem}\ell_{eff}$ describe the degrees to which TCE and H_2 react away in the membrane. Average values of $\varkappa^{mem}\ell_{eff}$ in tests with Pd/Al$_2$O$_3$, Pd/xGnP, and Pd-Au/xGnP catalysts were determined to be 4.95, 4.10, and 7.26 μm/s, respectively.

In most membranes suitable for practical separations, the length of the reactor, ℓ_{eff}, is not known. This is in part because of the complex morphology of the pore space (pore tortuosity and connectivity) and in part because most membranes are asymmetric. Thus, the detention time in the membrane reactor, $\frac{\ell_{eff}}{v}$ (s) is not known and computing the exact reaction rate constant k_{obs}^{mem} is not possible. For this reason, we quantify reactivity within the membrane reactor in terms of the reactive flux [17].

The normalized TCE reactive flux in membrane-based dehalogenation, $\hat{k}_{obs}^{mem}\ell_{eff}$ $((m/s)(M_{H2})^{-1} (g_{Pd}/ g_{PSf})^{-1})$, was computed by normalizing the measured reactive flux, $k_{obs}^{mem}\ell_{eff}$ $((m/s)(M_{H2})^{-1})$, by the mass loading of Pd in the polysulfone nanocomposite membrane (g_{Pd}/g_{PSf}). The H_2 reaction rate constants $\varkappa^{mem}$ and $\varkappa^{batch}$ are generally different; thus $\varkappa^{batch}$ and $\varkappa^{mem}\ell_{eff}$ were determined separately.

The reactive fluxes for membranes with embedded Pd/xGnP (2.56 ± 1.79 $(m/s)(M_{H2})^{-1}(g_{Pd}/g_{PSf})^{-1}$) and Pd-Au/xGnP (14.71 ± 5.96 $(m/s)(M_{H2})^{-1}(g_{Pd}/g_{PSf})^{-1}$) catalysts, were ~ 14 times and ~ 80 times higher than those for the membranes with commercial Pd/Al$_2$O$_3$ catalyst (0.18 ± 0.08 $(m/s)(M_{H2})^{-1}(g_{Pd}/g_{PSf})^{-1}$) (Figure 5).

3.3.1. Dehalogenation kinetics in a membrane reactor with a near-constant concentration of the reducing agent.

Under conditions of relatively slow decomposition of the reducing agent $(-\varkappa^{mem}t \ll 1)$ eq. 5a simplifies to the plug-flow model with the 1st order reaction:

$$0 = -v\frac{d[TCE]}{dx} - k_{obs}^{mem}[TCE][H_2]_0\exp(-\varkappa^{mem}t) \tag{5b}$$

$$\xrightarrow{\varkappa^{mem}t\to0} -v\frac{d[TCE]}{dx} - k_{1obs}^{mem}[TCE]$$

where k_{1obs}^{mem} is the observed 1st order rate constant in the membrane reactor. We note that for reactions where the reducing agent is reacting away sufficiently slowly $(\varkappa^{mem} \to 0)$, the 1st order kinetics can apply even when permeation is slow (i.e. small v) and the residence time (ℓ_{eff}/v) in the membrane is high:

$$\lim_{\varkappa^{mem}\ell_{eff}\to0} \frac{1 - exp(-\varkappa^{mem}\ell_{eff}/v)}{\varkappa^{mem}\ell_{eff}} = \frac{1}{v} \tag{8}$$

and

$$ln\frac{[TCE]}{[TCE]_0} = -k_{obs}^{mem}\ell_{eff}\frac{[H_2]_0}{\varkappa^{mem}\ell_{eff}}\{1 - exp(-\varkappa^{mem}\ell_{eff}/v)\} \tag{7b}$$

$$\xrightarrow{\varkappa^{mem}\ell_{eff}\to0} -\frac{k_{1obs}^{mem}\ell_{eff}}{v}$$

Practically, high permeate fluxes are needed, which requires fast kinetics of dehalogenation to reduce the concentration of a target pollutant even at a low residence time. Faster reduction reactions translate into faster consumption of the reducer. (i.e. larger $\varkappa^{mem}$)   Under these conditions, approximations (5b) and (7b) do not hold and 2nd order kinetics applies.

3.4. Resolving conflicting demands of throughput and reactivity within a membrane reactor

Although in the general case the plug-flow with 1st order reaction model given by eq.

(7b) [17] fits experimental results worse (see SM, section S3) than the plug flow with 2nd order reaction model described by eq. (7a), we applied the 1st order model to our membrane-based TCE dehalogenation data to elucidate the competition between mass transfer and reactivity within the membrane reactor (Table 2). The 1st order model is useful for a simple estimation of how effective different embedded catalysts are at different permeate fluxes: the 1st order reactive flux can be interpreted as the permeate flux for which the concentration of TCE is reduced in the membrane reactor by the factor of e$\cong$ 2.72.

At the transmembrane pressure of 0.69 bar, the average permeate flux through membranes with embedded Pd/Al$_2$O$_3$ was 15.5 L/(m^2·h), while the reactive flux was only 15.5 L/(m^2·h) leading to incomplete TCE reduction (Figure 5A). In contrast, at the same transmembrane pressure, the average permeate flux through the membranes with embedded Pd-Au/xGnP was 26.4 L/(m^2·h), and the reactive flux was 45.0 L/(m^2·h). Thus, using the Pd-Au/xGnP catalyst makes the membrane reaction feasible at permeate fluxes in the ultrafiltration range.

Table 2. Comparison of 1st order reactive flux[17] and volumetric permeate flux for membranes filled with one of the three catalysts studied: Pd/xGnP, Pd-Au/xGnP, and Pd/Al$_2$O$_3$ (baseline).

Embedded catalyst	TCE reactive flux for 1st order reaction model, $k_{1obs}^{mem}\ell_{eff}$, µm/s (L·m^{-2}·h^{-1})	Average volumetric permeate flux at ΔP = 2.76 bar, µm/s (L·m^{-2}·h^{-1})	Average volumetric permeate flux at ΔP = 0.69 bar, µm/s (L·m^{-2}·h^{-1})
Pd/Al$_2$O$_3$	1.8 (6.5)	24.9 (89.7)	4.3 (15.5)
Pd/xGnP	5.0 (18.0)	64.5 (232.2)	6.4 (23.2)
Pd-Au/xGnP	12.5 (45.0)	35.0 (125.9)	7.4 (26.4)

A comparison of batch and membrane-based reaction data (Figure 4B and Figure 5B), shows that the relative reactivity of Pd/xGnP catalyst with respect to Pd/Al$_2$O$_3$ decreased while for the Pd-Au/xGnP the ~ 80 fold advantage was maintained after

23

catalyst incorporation into membranes.   The decrease might be due to catalyst

occlusion by the surrounding polysulfone matrix of the nanocomposite membrane [17].

The occlusion effect can be mitigated by using a more permeable membrane [17] or by

selecting a cage-type catalyst support [36, 37] that limits or eliminates polymer access to

the catalyst.   It appears that the improvement in reactivity due to the addition of the

promoter metal (Pd/xGnP vs Pd-Au/xGnP, Figures 4B and 5B) is sufficient to

overcome the occlusion effect.   Remarkably, both Pd/xGnP and Pd-Au/xGnP

achieved >96% reduction of TCE while operating at 32 L/(m^2·h) and 14 L/(m^2·h)

respectively, compared to Pd/Al$_2$O$_3$ achieving only 80% reduction while operating at

16 L/(m^2·h) of TCE.

We conclude that the high reactivity of the Pd/xGnP and especially Pd-Au/xGnP

catalysts enables the application of reactive membranes for TCE dechlorination by

allowing for sufficient reaction time at high permeate fluxes.   By normalizing k_{obs}^{batch}

by Pd content in the batch reactor ((g$_{Pd}$/L)$^{-1}$) and normalizing $k_{obs}^{mem}\ell_{eff}$ by Pd

loading in the membrane (g$_{Pd}$/g$_{PSf}$) we show that Pd-Au/xGnP and Pd/xGnP are much

more cost-efficient than the commercial catalyst Pd/Al$_2$O$_3$ in dehalogenating TCE.

The reactivity of Pd/xGnP and Pd-Au/xGnP catalysts can be further improved by

optimizing particle size (to make better use of Pd surface atoms) and Pd:Au ratio.

Acknowledgements

25

List of Figures

List of Tables

References

1. B. P. Chaplin, M. Reinhard, W. F. Schneider, C. Schuth, J. R. Shapley, T. J. Strathmann and C. J. Werth, *Environ. Sci. Technol.*, 2012, **46**, 3655-3670.

2. R. Li, L. Zhang and P. Wang, *Nanoscale*, 2015, **7**, 17167-17194.

3. N. M. Julkapli and S. Bagheri, *Int. J. Hydrogen Energy*, 2015, **40**, 948-979.

4. P. V. Kamat, *J. Phys. Chem. Lett.*, 2010, **1**.

5. I. V. Lightcap, T. H. Kosel and P. V. Kamat, *Nano Lett.*, 2010, **10**, 577-583.

6. C. Huang, C. Li and G. Shi, *Energy Environ. Sci.*, 2012, **5**, 8848-8868.

7. G. Blanita and M. D. Lazar, *Micro and Nanosystems*, 2013, **5**, 138-146.

8. Z. Wei, R. Pan, Y. Hou, Y. Yang and Y. Liu, *Scientific Reports*, 2015, **5**, 15664.

9. Y. Li, X. B. Fan, J. J. Qi, J. Y. Ji, S. L. Wang, G. L. Zhang and F. B. Zhang, *Nano Res.*, 2010, **3**, 429-437.

10. J. Yang, C. G. Tian, L. Wang and H. G. Fu, *J. Mater. Chem.*, 2011, **21**, 3384-3390.

11. O. Metin, E. Kayhan, S. Ozkar and J. J. Schneider, *Int. J. Hydrogen Energy*, 2012, **37**, 8161-8169.

12. Y.-N. Kim, Y.-C. Lee and M. Choi, *Carbon*, 2013, **65**, 315-323.

13. K. Kyriaki, H. Fukushima and L. T. Drzal, *Comp. Part A: Appl. Sci. Manufact.*, 2007, **38**, 1675-1682.

14. J. Lu, L. T. Drzal, R. M. Worden and I. Lee, *Chem. Mater.*, 2007, **19**, 6240-6246.

15. J. Lu, I. Do, L. T. Drzal, R. M. Worden and I. Lee, *ACS Nano*, 2008, **2**, 1825-1832.

16. T. Maiyalagan, X. Wang and A. Manthiram, *RSC Adv.*, 2014, **4**, 4028-4033.

17. C. Crock, A. Rogensues, W. Shan and V. Tarabara, *Water Res.*, 2013, **47**, 3984-3996.

18. M. O. Nutt, K. N. Heck, P. Alvarez and M. S. Wong, *Appl. Catal. B - Environ.*, 2006, **69**, 115-125.

19.   M. O. Nutt, J. B. Hughes and M. S. Wong, *Environ. Sci. Technol.*, 2005, **39**, 1346-1353.

20.   J. Liu, F. He, E. Durham, D. Zhao and C. B. Roberts, *Langmuir*, 2008, **24**, 328-336.

21.   S. De Corte, T. Hennebel, J. P. Fitts, T. Sabbe, V. Biznuk, S. Verschuere, D. van der Lelie, W. Verstraete and N. Boon, *Environ. Sci. Technol.*, 2011, **45**, 8506-8513.

22.   U. Prusse and K. Vorlop, *J. Mol. Catal. A - Chem.*, 2001, **173**, 313-328.

23.   B. Schrick, J. L. Blough, A. D. Jones and T. E. Mallouk, *Chem. Mater.*, 2002, **14**, 5140-5147.

24.   C. C. Huang and H. L. Lien, *Water Sci. Technol.*, 2010, **62**, 202-208.

25.   A. Ghauch, H. Abou Assi, H. Baydoun, A. M. Tuqan and A. Bejjani, *Chem. Eng. J.*, 2011, **172**, 1033-1044.

26.   R. Abazari, F. Heshmatpour and S. Balalaie, *ACS Catal.*, 2013, **3**, 139-149.

27.   J. Xu and D. Bhattacharyya, *Ind. Eng. Chem. Res.*, 2007, **46**, 2348-2359.

28.   J. Xu and D. Bhattacharyya, *J. Phys. Chem. C*, 2008, **112**, 9133-9144.

29.   X. Y. Wang, C. Chen, H. L. Liu and J. Ma, *Water Res.*, 2008, **42**, 4656-4664.

30.   Y.-L. Fang, K. N. Heck, P. J. J. Alvarez and M. S. Wong, *ACS Catal.*, 2011, 128-138.

31.   M. W. Losey, M. A. Schmidt and K. F. Jensen, *Ind. Eng. Chem. Res.*, 2001, **40**, 2555-2562.

32.   F. Rossi, R. Cucciniello, A. Intiso, A. Proto, O. Motta and N. Marchettini, *AIChE J.*, 2015, **61**, 3511–3515.

33.   H. Wang, Z. Dong and C. Na, *ACS Sustainable Chem. Eng.*, 2013, **1**, 746-752.

34.   M. J. Moran, J. S. Zogorski and P. J. Squillace, *Environ. Sci. Technol.*, 2007, **41**, 74-81.

35.   I.-H. Do, 3331895, Michigan State University, 2006.

36.   N. Linares, C. P. Canlas, J. Garcia-Martinez and T. J. Pinnavaia, *Catal. Comm.*, 2014, **44**, 50-53.

37.   J. Dulebohn, P. Ahmadiannamini, T. Wang, S.-S. Kim, T. J. Pinnavaia and V. V.

Tarabara, *J. Membr. Sci.*, 2014, **453**, 478-488.

29